Biomimetic Synthesis of TiO$_2$−SiO$_2$−Ag Nanocomposites with Enhanced Visible-Light Photocatalytic Activity

Chuang Liu,[†] Dong Yang,[‡] Yang Jiao,[†] Yao Tian,[‡] Yuangui Wang,[‡] and Zhongyi Jiang*,[†]

[†]Key Laboratory for Green Technology of Ministry of Education, School of Chemical Engineering and Technology, Tianjin University, Tianjin 300072, China

[‡]Department of Biochemical Engineering and Key Laboratory of Systems Bioengineering of Ministry of Education, School of Chemical Engineering and Technology, Tianjin University, Tianjin, 300072, China

S Supporting Information

ABSTRACT: Ternary TiO$_2$−SiO$_2$−Ag nanocomposites with enhanced visible-light photocatalytic activity have been synthesized through a facile biomimetic approach by utilizing lysozyme as both inducing agent of TiO$_2$ and reducing agent of Ag$^+$. TiO$_2$ nanoparticles (∼280 nm) are at first fabricated by the inducing of lysozyme. Afterward, SiO$_2$ layers are formed as "pancakes" stuck out of TiO$_2$ nanoparticles through a sol−gel process. Finally, Ag nanocrystals (∼24.5 nm) are deposited onto the surface of TiO$_2$−SiO$_2$ composites via the reduction of lysozyme, forming TiO$_2$−SiO$_2$−Ag nanocomposites. The resultant nanocomposites display a high photocatalytic activity for the degradation of Rhodamine B under the visible-light irradiation, which can be attributed to the synergistic effect of enhanced photon absorption from the surface plasma resonance of Ag nanocrystals and the elevated adsorption capacity for Rhodamine B from the high specific surface area of SiO$_2$. This study may provide some inspiration for the rational design and the facile synthesis of composite catalysts with a high and tunable catalytic property through a green, efficient pathway.

KEYWORDS: biomimetic synthesis, TiO$_2$, Ag, nanocomposite, lysozyme, visible-light photocatalysis
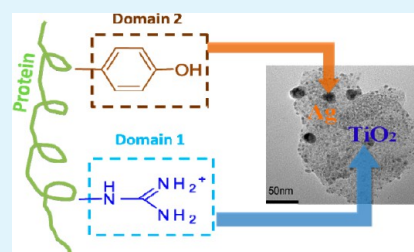
INTRODUCTION

It is well recognized that photocatalysis is an integrated process which involves optoelectronic conversion, surface/interface catalysis, and post-treatment or recycling of the photocatalyst.[1] In this regard, the composite photocatalyst, which can make full use of the synergistic effect of the constituents, should be rationally designed and efficiently synthesized to pursue the high and tunable photocatalytic performance.

TiO$_2$, a semiconductor photocatalyst, has attracted intense research attention in a broad range of applications, such as organic pollutants degradation, water splitting, and photovoltaic devices. However, as a single component, it has the low capacity for utilization of solar energy due to its large band gap and high recombination rate of photogenerated hole−electron pairs. To enhance the photocatalytic activity under the visible-light irradiation of TiO$_2$, a large number of binary TiO$_2$-based composite materials such as TiO$_2$−metal (Au, Ag, Pt),[2] TiO$_2$−SiO$_2$,[3] TiO$_2$−graphene nanocomposite,[4] and a small number of ternary nanocomposites such as TiO$_2$−SiO$_2$−Ag,[5] TiO$_2$−carbon−Ag,[6] TiO$_2$−graphene−Ag,[7] TiO$_2$−AgBr−Ag,[8] and TiO$_2$−graphene−Fe$_3$O$_4$[9] have been designed and synthesized. One popular approach for the synthesis of composite materials is the sol−gel method[10] based on the hydrolysis of titanium alkoxides, in which organic solvents, often alcohols, are added or liberated. Besides, conventional processes for depositing metal nanoparticles mainly encompass the chemical reduction, deposition−precipitation, photoinduced, and electrochemical method.[11] From the perspectives of green chemistry, an aqueous process is imperatively demanded for preparing the composite photocatalyst under the mild and controllable conditions.

Recently, much effort has been devoted to the biomimetic synthesis of metals and metal oxides, such as Au, Ag, SiO$_2$, TiO$_2$, ZrO$_2$, inspired by the biomineralization process in nature, an exquisite route to synthesize biominerals in organisms.[12−14] One distinct advantage of the biomimetic approach is that proteins and other biomolecules can implement fine and accurate control over the production of inorganic materials, such as size, shape, and crystal structure.[12] To date, a large number of natural and artificial proteins/peptides have been utilized for the synthesis of inorganic nanomaterials under mild conditions. Silicatein,[15] recombinant silaffins,[16] R5 peptide,[17] designed peptide,[18] protamine,[19] poly-L-lysine,[20] and bovine serum albumin (BSA)[21] have been utilized to induce the formation of TiO$_2$. BSA[22] and cytochrome C[23] has been utilized to reduce metal ions into metal nanoparticles (Au, Ag). In our previous study, it was found that lysozyme could induce the formation of ZrO$_2$[19] and TiO$_2$[24,25] nanoparticles. More recently, lysozyme has been used to induce the formation of TiO$_2$ nanoparticles[26] and reduce Au, Ag ions into the corresponding nanoparticles.[27,28] Therefore, lysozyme should be a versatile inducer/reducer for the green synthesis of composite nanomaterials, such as TiO$_2$−SiO$_2$−metal composites, due to its multifunctionalities. For instance,

Table 1. Preparation of Different TiO$_2$−SiO$_2$−Ag Nanocomposites Mediated by Lysozyme[a]

sample	Ti-BALDH (M)	Si$_2$O$_3^{2-}$ (mM)	Ag$^+$ (mM)	BET surface areas (m^{2}g^{-1})	photocatalytic activity[b] (h^{-1})
TiO$_2$	0.25	0	0	28.4	0.098
TiO$_2$−SiO$_2$	0.25	60	0	411.7	0.448
TiO$_2$−Ag	0.25	0	2	60.8	0.330
TiO$_2$−SiO$_2$(2)−Ag-1	0.25	60	0.5	370.5	0.726
TiO$_2$−SiO$_2$(2)−Ag-2	0.25	60	1	n.d.[c]	0.748
TiO$_2$−SiO$_2$(2)−Ag-3	0.25	60	2	n.d.[c]	0.841
TiO$_2$−SiO$_2$(1)−Ag-1	0.25	120	0.5	384.4	0.007
TiO$_2$−SiO$_2$(3)−Ag-1	0.25	30	0.5	152.6	2.345

[a]Different concentrations of precursors were used in preparing the nanocomposites: Ti-BALDH, Si$_2$O$_3^{2-}$, and Ag$^+$ were the precursors of TiO$_2$, SiO$_2$, and Ag, respectively. [b]Degradation rate constants of different photocatalysts under visible-light illumination. [c]None detected.

Scheme 1. (a) Schematic Illustration of Ternary TiO$_2$−SiO$_2$−Ag Nanocomposites with Enhanced Photocatalytic Activity under the Visible-Light Irradiation, (b) Amino Acid Sequence of Hen Egg Lysozyme,[a] and (c) Schematic Illustration for the Synthetic Route of TiO$_2$−SiO$_2$−Ag Nanocomposites Induced by Lysozyme[b]
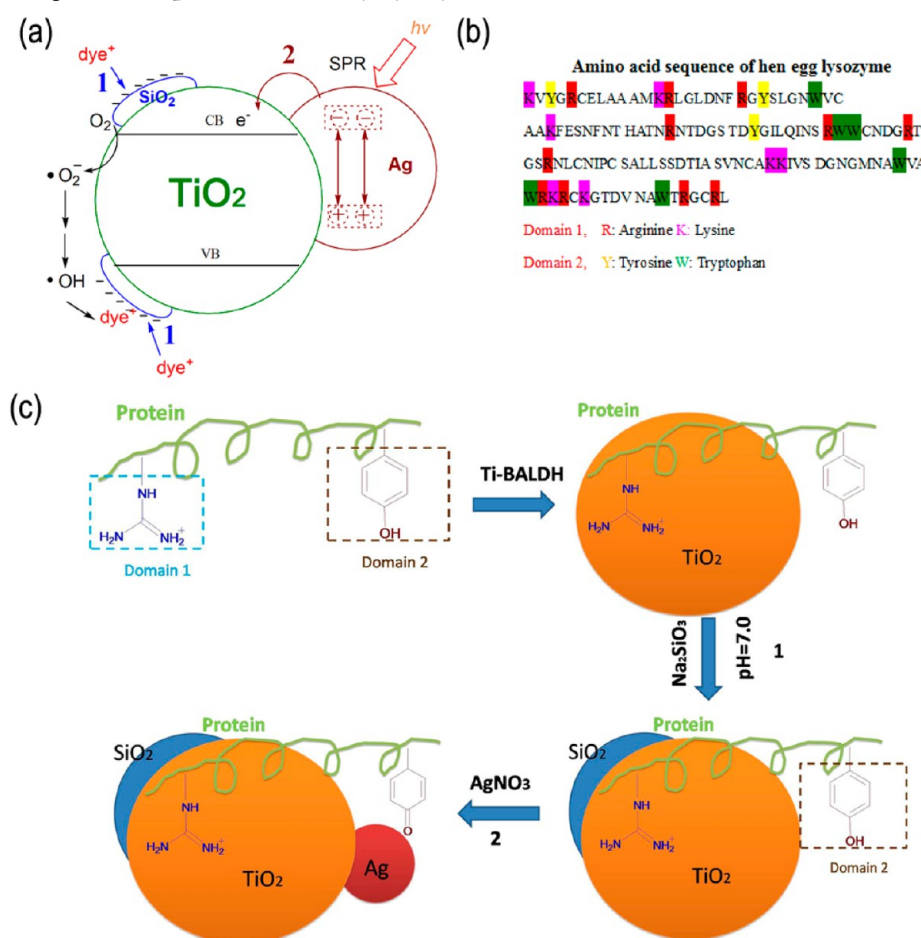
[a]Domain 1 represents the amino acid residues responsible for inducing the formation of TiO$_2$, and domain 2 represents the amino acid for reducing Ag$^+$. [b]Domain 1 is the arginine (R) residue, and domain 2 is the tyrosine (Y) residue (lysine and tryptophan residues are not shown).

hen egg lysozyme, a cationic polypeptide with a high isoelectric point (pI = 10.5) and with a large percentage of hydroxy- and imidazole-containing amino acid residues, such as arginine, lysine, tryptophan, and tyrosine residues, should meet the requirements for biomineralization-inducing and metal ion reduction.[27]

In this study, a facile and green approach to the synthesis of ternary TiO$_2$−SiO$_2$−Ag nanocomposites was developed by exploring the biomineralization-inducing capacity and the metal ion reduction capacity of lysozyme. The chemical compositions,

morphology, and physical and chemical structures of TiO$_2$−SiO$_2$−Ag nanocomposites were characterized. The photocatalytic performance of the prepared nanocomposites was evaluated using the degradation of Rhodamine B (RhB) as a model system under the visible-light irradiation. The photocatalytic mechanism was tentatively analyzed.

■ **EXPERIMENTAL SECTION**

Chemicals. Lysozyme (EC 3.2.1.17) and titanium(IV) bis-(ammonium lactato) dihydroxide (Ti-BALDH, a 50 wt % aqueous
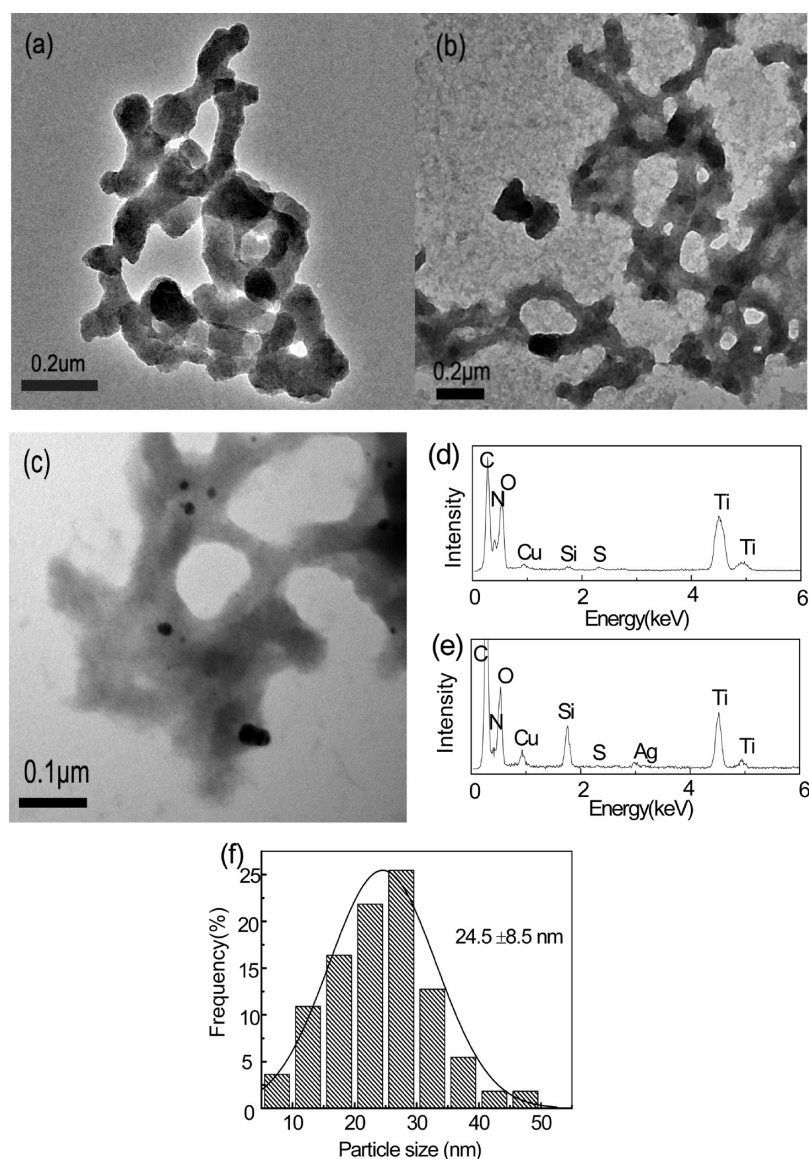
Figure 1. Typical TEM images of TiO_2-SiO_2-Ag induced by lysozyme at different synthetic steps: (a) TiO_2, (b) TiO_2-SiO_2, and (c) TiO_2-SiO_2-Ag; (d) EDS analysis of part b; (e) EDS analysis of part c. (f) The particle size histogram of Ag nanoparticles.

solution) were purchased from Sigma-Aldrich (Beijing, China). Silver nitrate ($AgNO_3$) and sodium silicate ($Na_2SiO_3·9H_2O$) were from Tianjin Guangfu Company. All chemicals were of analytic grade and used as received without further purification. Deionized water was used throughout the study.

Synthesis of TiO_2-SiO_2-Ag Nanocomposites. The synthesis of TiO_2-SiO_2-Ag nanocomposites can be divided into three steps. At first, TiO_2 nanoparticles were synthesized by using lysozyme as the inducer, following the procedure in the literature.[25] Briefly, 60 mL of a 5 mg mL^{-1} lysozyme solution was mixed with 60 mL of a 0.25 M Ti-BALDH solution, then agitated for 5 min at room temperature. Second, 120 mL of a Na_2SiO_3 solution (pH was adjusted to 7.0 with HNO_3) was added into the mixture and continuously stirred for 24 h to prepare the TiO_2-SiO_2 composites. The resultant precipitants were collected by centrifugation (8000 r/min) for 5 min and washed twice with water. At last, the TiO_2-SiO_2 composites were dispersed into a 50 mL of $AgNO_3$ solution and stirred for 24 h. The TiO_2-SiO_2-Ag composites were obtained by centrifugation (8000 r/min) for 10 min, rinsed with water twice, freeze-dried in a vacuum freeze drier for 24 h, and calcined at 500 °C for 2 h. A series of Na_2SiO_3 (30, 60, 120 mM) and $AgNO_3$ (0.5, 1, 2 mM) solutions with different concentrations were used to synthesize the TiO_2-SiO_2-Ag nanocomposites with different compositions. For

comparison, TiO_2, TiO_2-SiO_2, and TiO_2-Ag (Figure S1 in the Supporting Information) composite nanoparticles were prepared through the same procedure. All of the prepared samples and their physicochemical properties are listed in Table 1.

Characterization. Transmission electron microscopy (TEM) analysis of the samples was performed on a JEM-100CX II transmission electron microscope at an accelerating voltage of 200 kV. High-resolution transmission electron microscopy (HRTEM) and elemental mapping were conducted at 90 K using a JEOL-2011 equipped with a Bruker X-flash silicon drift detector (SDD) at 200 kV. The UV−vis absorption spectra of the samples were recorded using a UV−vis spectrophotometer (U-3010, Hitachi) equipped with an integration sphere for the diffuse-reflectance spectroscopy (DRS), and $BaSO_4$ was used as the reference. The X-ray photoelectron spectroscopy (XPS) of the samples was observed on a Perkin-Elmer PHI 1600 ESCA X-ray photoelectron spectroscope with a monochromatic Mg K_α radiation (1253.6 eV) and the binding energies were normalized to C1s peak at 284.6 eV. Agilent 7700x inductively coupled plasma mass spectrometry (ICP-MS) was used to determine the Ag fraction after the dissolution of the samples in HNO_3. X-ray diffraction (XRD) patterns were obtained with a Rigaku D/max 2500 V/PC X-ray diffractometer (Cu K_α, $\lambda = 0.154$ nm, 40 kV, 200 mA). Scattered radiation was detected in the angular
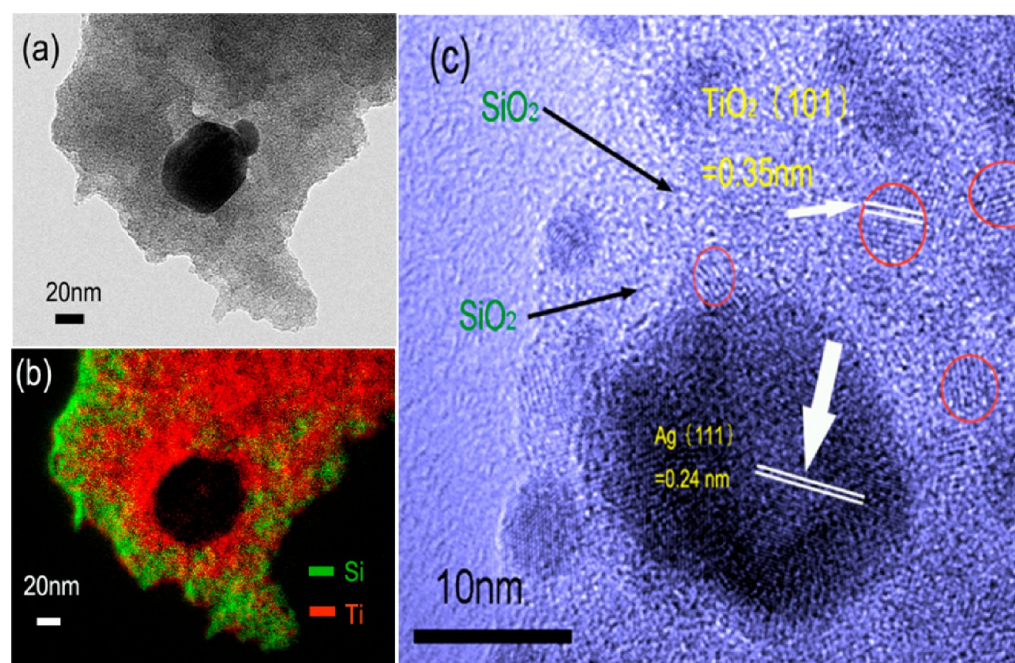
Figure 2. TEM image (a) and EDX elemental mapping (b) of TiO_2-SiO_2-Ag and HRTEM image (c) of TiO_2-SiO_2-Ag after calcination.

range of $10-90°$ (2θ) with a scan rate of $4°$ min^{-1}. FT-IR spectra of the samples were measured on a Nicolet-560 spectrometer. A total of 32 scans were accumulated with a resolution of 4 cm^{-1} for each spectrum. The Brunauer–Emmett–Teller (BET) surface area and Barrett–Joiner–Halenda (BJH) pore-size distribution measurement were tested on a TRISTAR-3000 surface area analyzer.

Measurement of Photocatalytic Activity. The photocatalytic degradation of RhB was used as a model system to evaluate the photocatalytic performance of TiO_2-SiO_2-Ag nanocomposites. Photocatalytic reactions were carried out in an 80 mL beaker. The reactive slurry containing 50 mg of catalysts and 50 mL of a 10 mg L^{-1} RhB solution was stirred in the dark for 0.5 h to ensure the saturated adsorption of RhB on the surface of the catalysts. For the visible-light irradiation experiment, a 150 W xenon arc lamp was used as the light source, and a cutoff filter was applied to block the UV light ($\lambda < 420$ nm). The reaction was performed under magnetic stirring without blowing any gas, and the distance between the xenon light and the reaction solution is 6 cm. At a defined time interval, the concentration of RhB in the suspension was analyzed using a UV–vis spectrophotometer at 553 nm, and the photocatalytic activity of the samples were calculated from the decrease amount of RhB.

■ RESULTS AND DISCUSSION

Synthesis of TiO_2-SiO_2-Ag Nanocomposites. As shown in Scheme 1a, TiO_2-SiO_2-Ag nanocomposites are designed to elevate the photocatalytic performance of TiO_2 in the visible-light region from two aspects: the deposition of Ag nanoparticles on the surface of TiO_2 is beneficial to harvest the visible-light energy by their plasmonic property;[29] the SiO_2 incorporation enhances the photocatalytic activity of TiO_2 through enlarging its specific surface area and, thus, increasing its adsorption capacity for dye based on the electrostatic attraction between negatively charged SiO_2 and positively charged RhB. Under the visible-light irradiation, the electron–hole pairs form first in Ag nanoparticles due to the SPR effect. Then, the photoexcited electrons transfer into the conduction band of TiO_2 and form $^\bullet O_2^-$ with O_2 and then $^\bullet OH$ radicals.[29] The positively charged RhB molecules are absorbed on the surface of TiO_2-SiO_2-Ag composites through the electronic interactions with negatively charged Si–OH groups. The resultant active radical species lead to the

degradation of RhB adsorbed on the surface of TiO_2-SiO_2- Ag. Meanwhile, the pre-enriched RhB molecules can also be excited by visible light, and then the photoinduced electrons inject into the conduction band TiO_2, triggering the photodegradation reactions.

When Ti-BALDH was added into the aqueous solution of lysozyme, the solution became turbid instantly and the white precipitates were formed within a few minutes. Scheme 1b shows the amino acid sequence of lysozyme, which includes 11 arginine, 7 lysine, 6 tryptophan, and 3 tyrosine residues. The lysine and arginine residues of lysozyme are able to induce the TiO_2 formation through the electrostatic interactions of amino groups with Ti-BALDH (Scheme 1c).[26] Subsequently, the hydrolysis of Na_2SiO_3 forms SiO_2 layer on the surface of TiO_2 particles through a sol–gel process, forming TiO_2-SiO_2 composites. Finally, when a $AgNO_3$ solution was added into the suspension of TiO_2-SiO_2 composites, the tryptophan, tyrosine, phenylalanine, and histidine residues of lysozyme are responsible for the reduction of Ag^+ to Ag.[28,30] The active sites of lysozyme responsible for the formation of TiO_2 is different from and independent of those for the reduction of Ag^+, indicating the feasibility of exploring this method to prepare a variety of composite materials by employing lysozyme as both inducer and reducer.

Figure 1 shows the typical characterization results of TiO_2-SiO_2-Ag at different synthetic steps. As demonstrated in Figure 1a, TiO_2 particles induced by lysozyme are highly interconnected nanoclusters and $\sim$280 nm in size measured by a dynamic light scattering method (Figure S1 in the Supporting Information). Then, the formed SiO_2 is like a "pancake" which sticks out of the TiO_2 nanoparticles (Figure 1b). The coverage of SiO_2 layers can be controlled by the Na_2SiO_3 amount: at the optimal Na_2SiO_3 amount, the SiO_2 layer forms on the surface of the TiO_2 nanoparticle, while considerable active sites of lysozyme can still be exposed for the generation of Ag nanoparticles; when the Na_2SiO_3 amount is excess, SiO_2 layers wrap up all the TiO_2 nanoparticles and thus hinder the generation of Ag nanoparticles. The presence of N and S elements in the EDS spectrum of

TiO$_2$−SiO$_2$ (Figure 1d) confirms the existence of lysozyme. One can clearly observe from Figure 1c the deposition of Ag nanoparticles on the surface of TiO$_2$−SiO$_2$ composites without obvious aggregation in TiO$_2$−SiO$_2$−Ag. The corresponding EDS analysis (Figure 1e) verifies the existence of Ag element in this sample. Before calcination, the nanoparticles link together via lysozyme molecules and form the interconnected clusters. After calcination, lysozyme molecules are removed and TiO$_2$ nanoparticles aggregate into bigger nanospheres. Uniform dispersion of Ag nanoparticles is beneficial for electron transfer from Ag to the conduction band of TiO$_2$. The particle-size histogram (Figure 1f) reveals that the particle size of Ag nanoparticles displays a normal distribution, and their average size is 24.5 ± 8.5 nm. The size of Ag nanoparticles is also crucial since the plasmonic effect is negligible when it is smaller than 2 nm or larger than 50 nm.[22] Thus, in this study, the plasmonic effect of Ag nanoparticles can be rationally manipulated.

In order to confirm the distribution of Ti and Si elements in TiO$_2$−SiO$_2$−Ag nanocomposites, a typical region is selected and shown in Figure 2a. The corresponding EDX elemental mapping (Figure 2b) manifests that the Ti element is mostly in the bulk of TiO$_2$−SiO$_2$−Ag nanocomposites, whereas the Si element is mostly on their edge. The HRTEM picture of TiO$_2$−SiO$_2$−Ag after calcination (Figure 2c) reveals that the spherical nanoparticle possesses a d-spacing value of 0.24 nm, corresponding to the (111) plane of Ag nanocrystals.[31] Meanwhile, (101) planes of anatase TiO$_2$ with lattice fringes of 0.35 nm are also observed aside the amorphous SiO$_2$ region. These results indicate that the designed synthetic route of TiO$_2$−SiO$_2$−Ag nanocomposites in this study is feasible and controllable.

Microstructure of TiO$_2$−SiO$_2$−Ag Nanocomposites. The microstructure of as-prepared TiO$_2$−SiO$_2$−Ag nanocomposites was characterized by XRD, TG, FT-IR, and XPS. XRD measurements were carried out to further confirm the formation of Ag nanocrystals and analyze the crystallization behavior of TiO$_2$. As shown in Figure 3a,b, the prepared TiO$_2$ and TiO$_2$−SiO$_2$ nanomaterials exhibit a weak broad peak around 25.2°, suggesting that TiO$_2$ is partially crystallized. After calcination at 500 °C for 2 h, all of the recorded peaks in the XRD patterns (Figure 3d) are assigned to the anatase TiO$_2$ (JCPDS No. 21-2172). For the TiO$_2$−SiO$_2$−Ag composite nanoparticles, two additional diffraction peaks appear at 38.1°
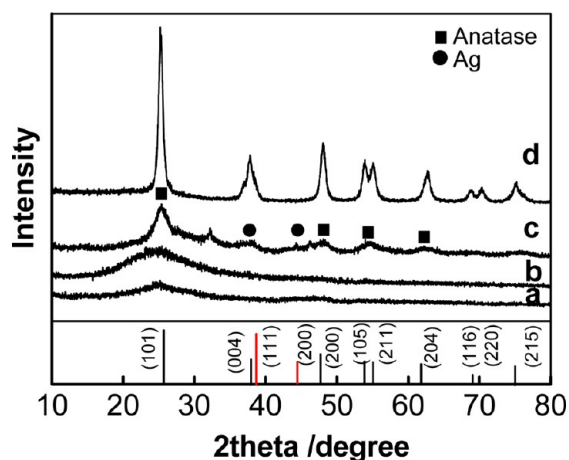
and 44.1° (Figure 3c), corresponding to the (111) and (200) plane of the face centered cubic (fcc) Ag crystal (JCPDS No. 65-2871). This result affirms that Ag nanoparticles are deposited onto the surface of TiO$_2$−SiO$_2$ composites.[31] On the basis of the full width at half-maximum (fwhm) of the (101) diffraction peak of TiO$_2$, the crystallized size of pure TiO$_2$ after calcination is calculated to be about 8.4 nm by the Debye−Scherrer formula.

FT-IR spectra were performed to analyze the composition of TiO$_2$, TiO$_2$−SiO$_2$, and TiO$_2$−SiO$_2$−Ag. As illustrated in Figure 4a, there are two peaks at 1650 and 1544 cm^{-1} in all the FT-IR
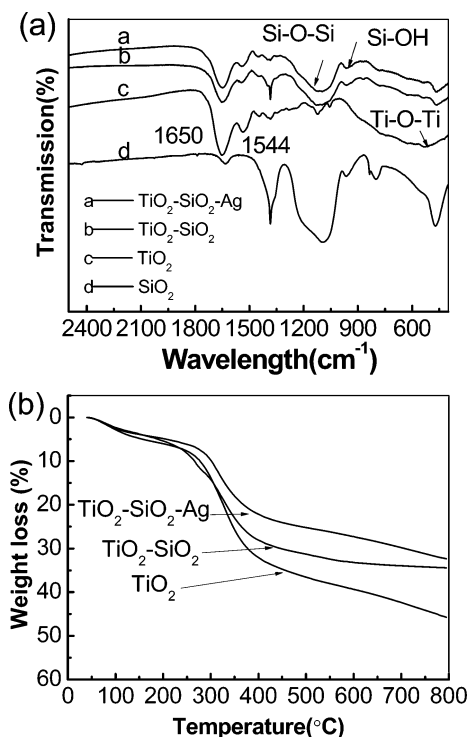
Figure 4. FT-IR spectra of TiO$_2$, SiO$_2$, TiO$_2$−SiO$_2$, and TiO$_2$−SiO$_2$−Ag (a); TG curves of TiO$_2$, TiO$_2$−SiO$_2$, and TiO$_2$−SiO$_2$−Ag (b).

spectra of TiO$_2$, TiO$_2$−SiO$_2$, and TiO$_2$−SiO$_2$−Ag, which are typical amide I and amide II absorption band of proteins (Figure S2 in the Supporting Information), respectively. This result testifies further that lysozyme is presented in the synthesized TiO$_2$. The peaks around 526 cm^{-1} are attributed to the Ti−O−Ti vibration in TiO$_2$. For SiO$_2$, TiO$_2$−SiO$_2$, and TiO$_2$−SiO$_2$−Ag, there are some peaks at the wavenumber of 1080−1105 cm^{-1} assigned to the asymmetric vibration of Si−O−Si and 940−960 cm^{-1} for the Si−OH vibration.[32] Figure 4b demonstrates the TG curve of TiO$_2$, TiO$_2$−SiO$_2$, and TiO$_2$−SiO$_2$−Ag. The major weight loss between 250 and 600 °C arises from the decomposition of the enzyme, which accounts for 45 wt %, 34 wt %, and 32 wt % in TiO$_2$, TiO$_2$−SiO$_2$, and TiO$_2$−SiO$_2$−Ag, respectively. The relative high amount of enzyme in TiO$_2$ is in favor of forming Ag nanoparticles or other components to construct composite materials. Moreover, the enzyme can be easily removed by calcination for the practical applications.

The X-ray photoelectron spectroscopy (XPS) was conducted to further confirm the chemical state of Ti, Si, and Ag atoms in the TiO$_2$−SiO$_2$−Ag nanocomposites. The C, O, N, Ti, Si, and Ag element can be found in the survey spectrum (Figure 5a). The high-resolution Ag 3d XPS spectrum (Figure 5b) has two peaks at 367.0 and 372.7 eV, which can be assigned to the Ag 3d$^5/_2$ and
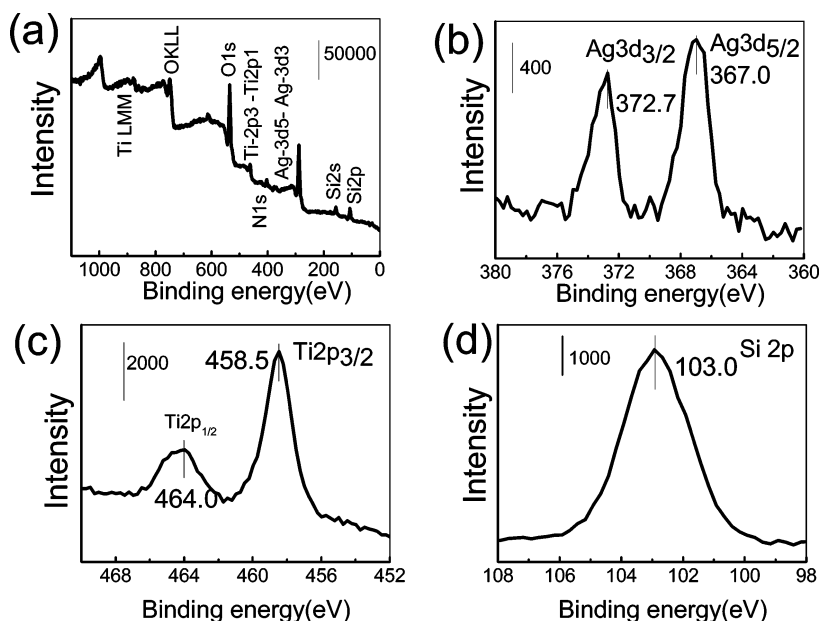
Figure 3. XRD patterns of TiO$_2$ (a) and TiO$_2$−SiO$_2$ (b) nanomaterials before calcination, and TiO$_2$−SiO$_2$−Ag (c) and TiO$_2$ (d) nanomaterials after calcined at 500 °C for 2 h (black line is anatase TiO$_2$, red line is Ag).

Figure 5. Survey (a), high-resolution Ag 3d (b), Ti 2p (c), and Si 2p (d) XPS spectrum of TiO_2−SiO_2−Ag.

Ag $3d^3/_2$ orbits, respectively. In the Ti 2p XPS spectrum (Figure 5c), two peaks are observed at 464.0 and 458.5 eV, which belong to Ti $2p^1/_2$ and Ti $2p^3/_2$, respectively. This result agrees well with Ti(IV) in pure anatase TiO_2 form. Figure 5d shows a Si 2p XPS spectrum with peaks at 103.0 eV, indicating the formation of a Si−O−Si bond.

In order to elucidate the role of SiO_2 in increasing the specific surface area, nitrogen adsorption−desorption isotherms of TiO_2, TiO_2−SiO_2, and TiO_2−SiO_2−Ag after calcination at 500 °C were conducted at liquid nitrogen temperature (77 K) and relative pressures (P/P_0) ranging from 0.00 to 1.00. According to the IUPAC classification,[33] the nitrogen adsorption−desorption isotherm of TiO_2 (Figure 6a) belongs to type IV with an H2 hysteresis loop. It contains a mesopore around 4.1 nm, on which

the adsorption proceeds via multilayer adsorption followed by capillary condensation.[33] It is deduced that the pores are produced when the occluded lysozyme (about 3−4 nm) molecules are removed by calcination. The H2 hysteresis loop at low relative pressure ($0.4 < P/P_0 < 0.7$) is often observed for porous inorganic oxides, which can be ascribed to the pore connectivity effect. Whereas, nitrogen adsorption−desorption isotherms of TiO_2−SiO_2 and TiO_2−SiO_2−Ag (Figure 6b) are categorized to type I with nitrogen adsorption completed at the low pressure region ($P/P_0 < 0.5$). This result is an indicative of the adsorption in micropores. The occurrence of the H4 hysteresis loop in TiO_2−SiO_2−Ag may be attributed to narrow slitlike pores caused by the deposition of Ag nanoparticles while there is no hysteresis loop in the TiO_2−SiO_2 sample.[33] The BET surface areas of TiO_2−SiO_2 and TiO_2−SiO_2−Ag after calcination are 411.7 and 370.5 $m^2 g^{-1}$, which are 14.5 and 13.0 times higher than that of TiO_2 (28.4 $m^2 g^{-1}$), respectively. Compared with other TiO_2 composite materials in the literature (100−300 m^2 g^{-1}),[34,35] the specific surface areas in this study are still at a high level. These results demonstrate that the formation of SiO_2 significantly increases the surface area, while the addition of Ag slightly decreases the surface area because a part of the pores may be blocked by the deposited Ag nanoparticles. Besides, there are almost no pores in Ag nanoparticles.

Photocatalytic Activity of TiO_2−SiO_2−Ag Nanocomposites. DRS spectra were conducted to assess the optical property of prepared TiO_2−SiO_2−Ag nanocomposites. As illustrated in Figure 7, TiO_2 and TiO_2−SiO_2 have little absorption between 400 and 800 nm. While in the DRS spectra of TiO_2−Ag and TiO_2−SiO_2−Ag, a notable absorption in the visible-light region can be observed with a peak around 480 nm, which is principally due to the SPR effect of Ag nanocystals.[36] For all the samples, the optical absorption threshold of the TiO_2 bandgap transition remains almost unchanged, indicating that Ag and SiO_2 are not doped into the crystal lattice of TiO_2 by this biomimetic method. In order to evaluate the effect of the Ag amount on the photocatalytic activity of TiO_2−SiO_2−Ag nanocomposites, three samples containing 0.04%, 0.08%, and 0.11% Ag determined by ICP were prepared. It is noted that the Ag dosage is much lower
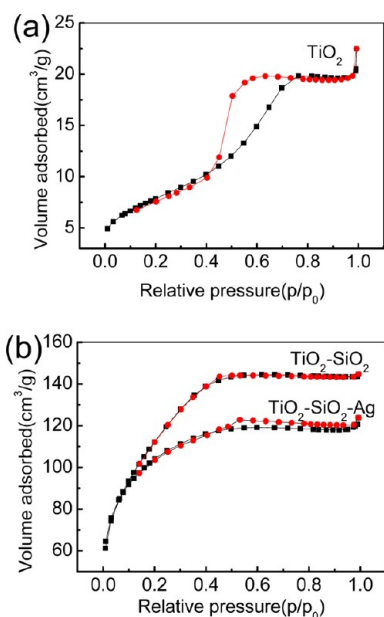

Figure 6. Nitrogen adsorption−desorption isotherms of TiO_2 (a), TiO_2−SiO_2, and TiO_2−SiO_2−Ag (b) after calcination at 500 °C for 2 h.
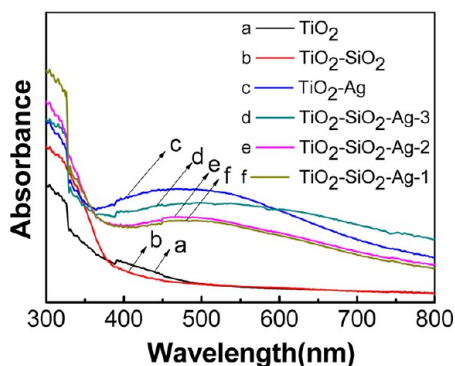
Figure 7. DRS spectra of TiO_2, TiO_2-SiO_2, TiO_2-Ag, and TiO_2-SiO_2-Ag.

than that in the literature (approximately 1−5 wt %),[37] which can be assigned to the low content and reducing capacity of lysozyme. The absorbance intensity gradually enhances with the increase of the Ag content in the TiO_2-SiO_2-Ag, endowing the photocatalyst higher absorbance of visible light.

The photodegradation of RhB dye was catalyzed by TiO_2-SiO_2-Ag under the visible-light irradiation ($\lambda > 420$ nm) to evaluate its photocatalytic activity. TiO_2-SiO_2-Ag powders were mixed with the RhB solution and agitated in the dark for 0.5 h to reach the adsorption equilibrium (Figure S3 in the Supporting Information). The change of the RhB concentration during the photodegradation process is shown in Figure 8a. It is noted that about 35% of RhB molecules are adsorbed on the surface of TiO_2-SiO_2-Ag when the adsorption reaches equilibrium in the dark, while only 10% of RhB molecules are adsorbed on TiO_2-Ag and TiO_2. This is explained by that the Si−OH groups on the surface of TiO_2-SiO_2-Ag can bind carboxylic groups of RhB dominantly through a monodentate ester-like linkage.[38] After the visible-light irradiation for 4 h, the

dyes are almost degraded by TiO_2-SiO_2-Ag, which is higher than those by TiO_2-Ag (80%) and TiO_2 (30%).

The natural logarithm of the absorbance vs the irradiation time is plotted and displayed in Figure 8b. Obviously, the degradation process obeys the pseudofirst-order kinetics, in accordance with the literature.[39] The degradation rates of RhB by different photocatalysts are calculated and listed in Table 1. As we can see, the degradation rates of TiO_2, TiO_2-SiO_2, and TiO_2-Ag are 0.098 h^{-1}, 0.448 h^{-1}, and 0.330 h^{-1}, respectively. The contributions of SiO_2 and Ag for the degradation rate are 0.35 and 0.232 h^{-1}, respectively. If the TiO_2-SiO_2-Ag nanocomposite is only the physical mixture of TiO_2, SiO_2, and Ag nanoparticles, its degradation rate should be about 0.68 h^{-1}. However, the degradation rates of prepared TiO_2-SiO_2 (2)-Ag(1,2,3) nanocomposites (0.726, 0.748, 0.841 h^{-1}) are larger than this value in fact. Therefore, it is concluded that both the deposition of Ag and the doping of SiO_2 render significantly elevated photocatalytic activity of TiO_2 under the visible light, and a synergistic effect exists apparently due to the coexistence of SiO_2 and Ag in TiO_2.

As shown in Figure 8c, the photocatalytic rate of TiO_2-SiO_2-Ag increases slightly as the Ag content increases. It is reported that the deposition of noble metals has an optimal amount[34] because the noble metals can also serve as the recombination center of photoinduced carriers and reduce the crystallinity of TiO_2,[37] thus lowering the photocatalytic activity of TiO_2 photocatalysts. This can explain the lower content of Ag chosen in our experiments. In addition, the amount of SiO_2 exerts a significant influence on the photoactivity of the catalyst. TiO_2-SiO_2-Ag-1 photocatalysts with different SiO_2 contents were prepared, and their photocatalytic performance under the visible-light irradiation for 1 h was measured. The degradation rate order is as follows: $TiO_2-SiO_2(3)-Ag-1$ (96.9%) > $TiO_2-SiO_2(2)-Ag-1$ (67.5%) > TiO_2-Ag-1 (31.0%) > TiO_2-SiO_2 (1)-Ag-1 (1.0%). This result demonstrates that an optimal SiO_2 content can
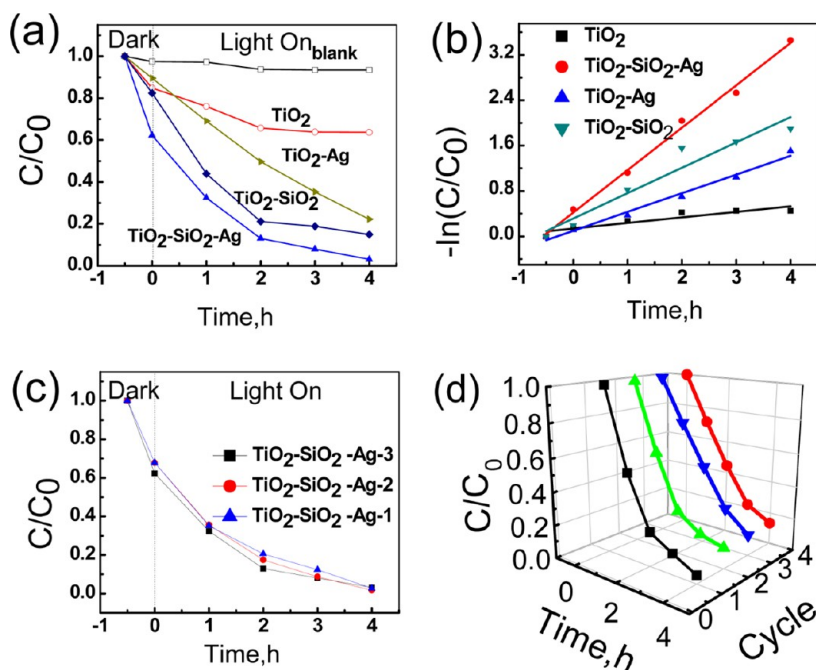

Figure 8. (a) Photocatalytic degradation of RhB without any catalyst and with TiO_2, TiO_2-Ag, TiO_2-SiO_2, and TiO_2-SiO_2-Ag as the catalyst under visible light, (b) kinetic study of the photocatalytic degradation of RhB, (c) photocatalytic degradation of RhB catalyzed by TiO_2-SiO_2-Ag with different silver loadings, and (d) four cycles of the photocatalytic degradation of RhB catalyzed by TiO_2-SiO_2-Ag-1 under the visible-light irradiation.

drastically enhance the degradation rate, while the excess of SiO_2 may cover up the TiO_2 regions and hinder the direct contact of TiO_2 with the dyes, resulting in low photocatalytic activity.

The recycling stability of prepared TiO_2-SiO_2-Ag photocatalysts was evaluated by using TiO_2-SiO_2-Ag-1 as the representative. After each photocatalytic reaction cycle, the photocatalysts were recovered by centrifugation, washed with deionized water, and transferred into a fresh solution of RhB to undergo the reaction under identical conditions. It can be observed from Figure 8d the photocatalytic activity remains almost unchanged after four consecutive recycles, confirming the strong chemical stability of TiO_2-SiO_2-Ag photocatalysts.

Photocatalytic Degradation Mechanism of RhB. It is well accepted that the photocatalytic degradation of RhB occurs via two competitive processes:[40] the N-demethylation process and the destruction of the conjugated structure. As shown in Figure 9c, the maximum absorption of RhB catalyzed by TiO_2-
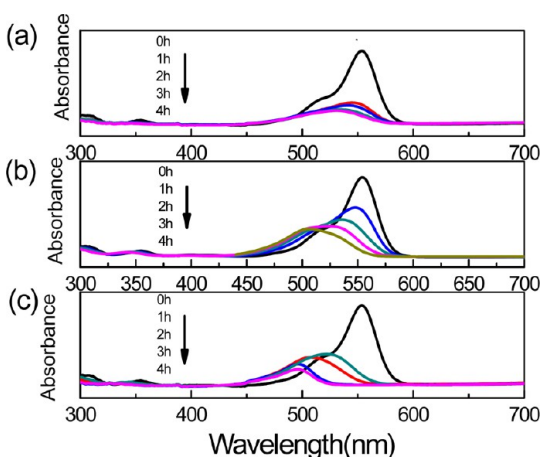

Figure 9. UV−visible spectrum changes of RhB over TiO_2-Ag (a), TiO_2-SiO_2 (b), and TiO_2-SiO_2-Ag (c) photocatalysts.

SiO_2-Ag decreases from 553 to 522, 510, and 496 nm with the increase of the reaction time. Meanwhile, the color of the reactive suspension changes gradually from pink to light green with the time elapsing. This hypsochromic shift of the absorption band is ascribed to the formation of a series of N-deethylated intermediates in a stepwise manner.[41] The absorption peaks at 522, 510, and 496 nm are identified as *N,N*-diethyl rhodamine (DER), *N*-ethyl rhodamine (MER), and rhodamine,[42] respectively. In the reaction system using TiO_2-Ag as the photocatalyst, however, the absorption peak shifts from 553 to 533 nm with the increase of the reaction time (Figure 9a). Meanwhile, the color of the reaction suspension changes gradually from pink to light red. The peak at 533 nm is identified as *N,N,N*-triethyl rhodamine (TER). In the case of TiO_2-SiO_2 used as the photocatalyst, RhB is unexpectedly degraded to a great extent, and the maximum adsorption peak shifts from 553 to 534, 522, and 510 nm (Figure 9b), similar to that using TiO_2-SiO_2-Ag as the photocatalyst. This result indicates that the formation of SiO_2 changes the photodegradation rate of RhB and the degradation pathway of RhB simultaneously. Since the N-deethylation reaction of RhB is usually observed as a surface reaction induced by the oxygen species (ROS) on the catalyst, it occurs easily in the reaction systems containing TiO_2-SiO_2-Ag and TiO_2-SiO_2 with high specific surface area. Nevertheless, the destruction of the conjugated structure of RhB becomes the main process

instead of the N-demethylation process, due to the low specific surface of TiO_2-Ag.

CONCLUSIONS

In summary, a biomimetic approach is first developed for the synthesis of the ternary TiO_2-SiO_2-Ag nanocomposite photocatalyst by utilizing lysozyme as both inducing agent of TiO_2 and reducing agent of Ag^+. The resultant TiO_2-SiO_2-Ag nanocomposites exhibit high, stable, and tunable photocatalytic activity in catalyzing the decomposition of RhB under the visible-light radiation, which can be attributed to the synergistic effect of the enhanced light harvesting ability from plasmonic Ag nanoparticles and enhanced adsorption capacity of RhB from SiO_2 moiety. This study may endow a facile, green approach to the synthesis of nanocomposite materials by rational design and choice of biomolecules with multifunctionalities, such as catalysis, redox, and templating.

ASSOCIATED CONTENT

Ⓢ Supporting Information
TEM images of lysozyme-synthesized Ag nanoparticles, TiO_2- Ag and SiO_2 formed through the sol−gel process, TiO_2 particle distribution measured by the DLS method, FT-IR of lysozyme, adsorption of RhB at room temperature with time on TiO_2, TiO_2-SiO_2, and TiO_2-SiO_2-Ag photocatalysts. This material is available free of charge via the Internet at http://pubs.acs.org.

AUTHOR INFORMATION

Corresponding Author
*Phone: +86-22-23500086. E-mail: zhyjiang@tju.edu.cn.

Author Contributions
The manuscript was written through contributions of all authors. All authors have given approval to the final version of the manuscript.

Notes
The authors declare no competing financial interest.

REFERENCES

(1) Tong, H.; Ouyang, S.; Bi, Y.; Umezawa, N.; Oshikiri, M.; Ye, J. *Adv. Mater.* **2012**, 24, 229−251.
(2) Chen, S. F.; Li, J. P.; Qian, K.; Xu, W. P.; Lu, Y.; Huang, W. X.; Yu, S. H. *Nano Res.* **2010**, 3, 244−255.
(3) Yang, D.; Chen, C.; Zheng, Z.; Liu, H.; Waclawik, E. R.; Yan, Z.; Huang, Y.; Zhang, H.; Zhao, J.; Zhu, H. *Energy Environ. Sci.* **2011**, 4, 2279−2287.
(4) Liang, Y.; Wang, H.; Sanchez Casalongue, H.; Chen, Z.; Dai, H. *Nano Res.* **2010**, 3, 701−705.
(5) Chen, Q.; Shi, H.; Shi, W.; Xu, Y.; Wu, D. *Catal. Sci. Technol.* **2012**, 2, 1213−1220.
(6) Zhang, P.; Shao, C.; Zhang, Z.; Zhang, M.; Mu, J.; Guo, Z.; Sun, Y.; Liu, Y. *J. Mater. Chem.* **2011**, 21, 17746−17753.
(7) Wen, Y.; Ding, H.; Shan, Y. *Nanoscale* **2011**, 3, 4411−4417.
(8) Tian, G.; Chen, Y.; Bao, H.-L.; Meng, X.; Pan, K.; Zhou, W.; Tian, C.; Wang, J.-Q.; Fu, H. *J. Mater. Chem.* **2012**, 22, 2081.

(9) Lin, Y.; Geng, Z.; Cai, H.; Ma, L.; Chen, J.; Zeng, J.; Pan, N.; Wang, X. *Eur. J. Inorg. Chem.* **2012**, *2012*, 4439−4444.

(10) Chen, D.; Yang, D.; Wang, Q.; Jiang, Z. *Ind. Eng. Chem. Res.* **2006**, *45*, 4110−4116.

(11) Wang, X.; Dornom, T.; Blackford, M.; Caruso, R. A. *J. Mater. Chem.* **2012**, *22*, 11701−11710.

(12) Dickerson, M. B.; Sandhage, K. H.; Naik, R. R. *Chem. Rev.* **2008**, *108*, 4935−4978.

(13) Liu, C.; Wang, Y.; Geng, J.; Jiang, Z.; Yang, D. *Prog. Chem.* **2011**, *23*, 2510−2521.

(14) Liu, C.; Yang, D.; Wang, Y.; Shi, J.; Jiang, Z. *J. Nanopart. Res.* **2012**, *14*, 1−12.

(15) Sumerel, J. L.; Yang, W.; Kisailus, D.; Weaver, J. C.; Choi, J. H.; Morse, D. E. *Chem. Mater.* **2003**, *15*, 4804−4809.

(16) Kröger, N.; Dickerson, M. B.; Ahmad, G.; Cai, Y.; Haluska, M. S.; Sandhage, K. H.; Poulsen, N.; Sheppard, V. C. *Angew. Chem., Int. Ed.* **2006**, *118*, 7397−7401.

(17) Sewell, S. L.; Wright, D. W. *Chem. Mater.* **2006**, *18*, 3108−3113.

(18) Zhao, C.-X.; Yu, L.; Middelberg, A. P. J. *RSC Adv.* **2012**, *2*, 1292−1295.

(19) Jiang, Y.; Yang, D.; Zhang, L.; Li, L.; Sun, Q.; Zhang, Y.; Li, J.; Jiang, Z. *Dalton Trans.* **2008**, 4165−4171.

(20) Hawkins, K. M.; Wang, S. S. S.; Ford, D. M.; Shantz, D. F. *J. Am. Chem. Soc.* **2004**, *126*, 9112−9119.

(21) Coradin, T.; Coupé, A.; Livage, J. *Colloids Surf., B* **2003**, *29*, 189−196.

(22) Xie, J.; Zheng, Y.; Ying, J. Y. *J. Am. Chem. Soc.* **2009**, *131*, 888−889.

(23) Bakshi, M. S.; Kaur, H.; Banipal, T. S.; Singh, N.; Kaur, G. *Langmuir* **2010**, *26*, 13535−13544.

(24) Zhang, Y.; Wu, H.; Li, J.; Li, L.; Jiang, Y.; Jiang, Z. *Chem. Mater.* **2007**, *20*, 1041−1048.

(25) Chen, G.; Li, M.; Li, F.; Sun, S.; Xia, D. *Adv. Mater.* **2010**, *22*, 1258−1262.

(26) Luckarift, H. R.; Dickerson, M. B.; Sandhage, K. H.; Spain, J. C. *Small* **2006**, *2*, 640−643.

(27) Eby, D. M.; Schaeublin, N. M.; Farrington, K. E.; Hussain, S. M.; Johnson, G. R. *ACS Nano* **2009**, *3*, 984−994.

(28) Das, R.; Jagannathan, R.; Sharan, C.; Kumar, U.; Poddar, P. *J. Phys. Chem. C* **2009**, *113*, 21493−21500.

(29) Linic, S.; Christopher, P.; Ingram, D. B. *Nat. Mater.* **2011**, *10*, 911−921.

(30) Tan, Y. N.; Lee, J. Y.; Wang, D. I. C. *J. Am. Chem. Soc.* **2010**, *132*, 5677−5686.

(31) Tang, Y.; Subramaniam, V. P.; Lau, T. H.; Lai, Y.; Gong, D.; Kanhere, P. D.; Cheng, Y. H.; Chen, Z.; Dong, Z. *Appl. Catal. B-Environ.* **2011**, *106*, 577−585.

(32) Jung, K. Y.; Park, S. B. *Appl. Catal., B: Environ.* **2000**, *25*, 249−256.

(33) Kruk, M.; Jaroniec, M. *Chem. Mater.* **2001**, *13*, 3169−3183.

(34) Zhao, W.; Feng, L.; Yang, R.; Zheng, J.; Li, X. *Appl. Catal., B: Environ.* **2011**, *131*, 181−189.

(35) Joo, J. B.; Zhang, Q.; Lee, I.; Dahl, M.; Zaera, F.; Yin, Y. *Adv. Funct. Mater.* **2012**, *22*, 166−174.

(36) Zhang, H.; Fan, X.; Quan, X.; Chen, S.; Yu, H. *Environ. Sci. Technol.* **2011**, *45*, 5731−5736.

(37) Zhang, Q.; Lima, D. Q.; Lee, I.; Zaera, F.; Chi, M.; Yin, Y. *Angew. Chem., Int. Ed.* **2011**, *123*, 7226−7230.

(38) Dong, W.; Lee, C. W.; Lu, X.; Sun, Y.; Hua, W.; Zhuang, G.; Zhang, S.; Chen, J.; Hou, H.; Zhao, D. *Appl. Catal., B: Environ.* **2010**, *95*, 197−207.

(39) Su, C.; Liu, L.; Zhang, M.; Zhang, Y.; Shao, C. *CrystEngComm* **2012**, *14*, 3989−3999.

(40) Chen, C.; Zhao, W.; Li, J.; Zhao, J.; Hidaka, H.; Serpone, N. *Environ. Sci. Technol.* **2002**, *36*, 3604−3611.

(41) Lei, P.; Chen, C.; Yang, J.; Ma, W.; Zhao, J.; Zang, L. *Environ. Sci. Technol.* **2005**, *39*, 8466−8474.

(42) Fu, H.; Zhang, S.; Xu, T.; Zhu, Y.; Chen, J. *Environ. Sci. Technol.* **2008**, *42*, 2085−2091.